

Dynamics of mesoscopic polarization in the uniaxial tetragonal tungsten bronze $(\text{Sr}_x\text{Ba}_{1-x})\text{Nb}_2\text{O}_6$ Elena Buixaderas ^{1,*}, Martin Kempa ¹, Šarūnas Svirskas², Christelle Kadlec ¹,
Viktor Bovtun ¹, Maxim Savinov¹, Marek Paściak¹ and Jan Dec ³¹*Institute of Physics of the Czech Academy of Sciences, Na Slovance 2, 18221 Prague, Czech Republic*²*Faculty of Physics, Vilnius University, Saulėtekio al. 9, LT-10222 Vilnius, Lithuania*³*Institute of Materials Science, University of Silesia, PL-40-007 Katowice, Poland*

(Received 24 July 2019; revised manuscript received 30 September 2019; published 27 November 2019)

The high-frequency dielectric behavior of uniaxial tungsten-bronze strontium barium niobate crystals with various Sr/Ba ratios, including both ferroelectric and relaxor compositions, have been studied in a broad frequency range (10^4 to 10^{13} Hz) and temperature interval 100–500 K in order to thoroughly understand the evolution of the relaxation dynamics across the ferroelectric phase transition. The dielectric response along the polar axis consists of three relaxations corresponding to polarization mechanisms related to several correlation lengths of mesoscopic order. All of them show dissimilar behaviors with temperature, pointing out to their distinct nature. A temperature-dependent central mode at THz frequencies and a relaxation above 10 GHz are accompanied by the slowing down of a relaxation in the MHz range. This response reveals the complex mechanism of the phase transition and supports the coexistence of displacive and order-disorder scenarios. Relaxor and ferroelectric compositions surprisingly reveal similar qualitative behavior within the frequency window used. However, relaxor crystals display relaxations at higher frequency because of the smaller extent of the polar fluctuations and ferroelectric regions, which coexist in almost all the compositions. The presence of two different ferroelectric subsystems in the structure agrees with the existence of several polarization mechanisms involved in the complex dielectric and ferroelectric response.

DOI: [10.1103/PhysRevB.100.184113](https://doi.org/10.1103/PhysRevB.100.184113)**I. INTRODUCTION**

Within the tetragonal tungsten-bronze (TTB) family [1], strontium barium niobate $\text{Sr}_x\text{Ba}_{1-x}\text{Nb}_2\text{O}_6$ (SBN) is the best candidate to decipher the origin of the transformation from ferroelectric to relaxor behavior and to relate it to the intrinsic disorder existing in the structure. Despite being one of the most fruitful structures in creating targeted dielectric, piezoelectric, and electro-optical properties [2–4], the TTB structure, due to its complexity in comparison to the perovskite one, has been much less studied. Unlike cubic perovskites, the TTB structure is not isotropic in its parent paraelectric phase, showing a preferential axis along which, depending on temperature and composition, the ferroelectric or the relaxor behavior manifests. On the other hand, in the direction perpendicular to it, the dielectric response is almost invariable with temperature, and the crystalline structure exhibits peculiar deviations from the average structure, mainly seen in the diffuse scattering patterns and in the incommensurate positions of the oxygen atoms [5].

The relationship between the structure and the properties in this family is very intricate; however microscopic models are still very seldom. This is due to the difficulties to handle such a big unit cell— $(\text{Sr}, \text{Ba})_5\text{Nb}_{10}\text{O}_{30}$ —in calculations and simulations where, in addition, several unit cells have to be taken into account to mimic reasonably the disordered distribution of cations. As in all TTBs, the SBN structure is

based on a network of corner-sharing NbO_6 octahedra, which are arranged forming three types of channels along the polar c axis, with different site symmetries and occupied by different atoms. In SBN with $x > 0.33$, the squared channels (A1 site) are occupied by Sr, the pentagonal ones (A2 site) by Sr and Ba, and the triangular channels (C site) are empty [6,7] (see Fig. 1). The occupation of the channels is not complete, and a significant amount of vacancies is present in both A1 and A2 sites, therefore SBN is an archetype of unfilled TTB, which crystallizes in the tetragonal variation for the compositional range $0.32 < x < 0.82$ [8]. There are two types of oxygen octahedra depending on the site symmetry of the central Nb atom: Nb(1) has mm symmetry and just 2 out of 10 Nb in the unit cell occupy this position, leaving these octahedra isolated (called “linking octahedra”), while Nb(2) possesses 1 symmetry, and their octahedra form perovskite subunits within the framework of the TTB unit cell (Fig. 1). The mentioned complexity of TTB structure stimulates fruitfully the development of experimental techniques and a proper elaboration of experimental data.

SBN is known as a system displaying an almost perfect tunability from ferroelectric to relaxor behavior depending on composition (crystals with more than $\sim 50\%$ Sr show already mixed ferroelectric-relaxor properties) [9]. In addition, the crystal with 61% of Sr (SBN-61) shows maximal values of the permittivity and was intensively studied due to its photorefractive properties when doped with cerium [3]. For the ferroelectric samples, the phase transition on cooling takes place during a transformation from the centrosymmetric space group $P4/mbm$ [10–12] to the polar space group $P4bm$ [7,12]

*buixader@fzu.cz

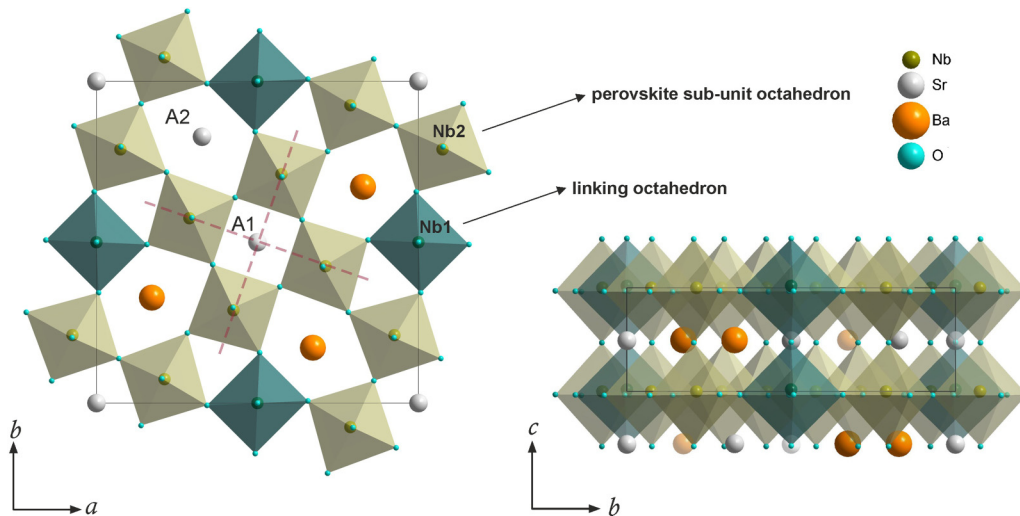


FIG. 1. Structure of SBN in ab and bc planes. Dashed red lines mark the perovskite subunit (lighter-colored octahedra $\text{Nb}(2)\text{O}_6$ within the TTB unit cell in solid gray lines). Linking oxygen octahedra $\text{Nb}(1)\text{O}_6$ are shown in blue color.

and below T_C , the spontaneous polarization develops along the tetragonal c axis. Depending on the crystallization method, and especially for higher amounts of Sr, an orthorhombic distortion appears [1,6,13].

Recent simulations have related the appearance of ferroelectricity in TTBs to the displacement of Nb atoms, which is severely influenced by the cation distribution in the channels and the distortion of the octahedral network [14]. The shift of Nb atoms is not gradual with temperature and does not rise to a proper soft mode, due to the complexity of the Nb interaction with the surrounding oxygen octahedra, which prevents such a simple mechanism. Relaxor properties are also indirectly linked to the tilts of the octahedra and their deformations, due to the random occupancy of the squared and pentagonal channels [15].

The dielectric behavior has been studied in several SBN crystals using a broadband approach (from 10^2 to 10^{13} Hz) [12,16,17]. The picture that came out from these studies revealed that there is not only one single polar mechanism responsible for the phase transition and its strong permittivity maximum, as in other ferroelectric materials. Instead, various excitations with characteristic frequencies ranging from the THz down to, at least, the kHz range were found. Notwithstanding the ferroelectric or relaxor character of the SBN crystals, the coexistence of polar regions with different mesoscopic order seems to be responsible for the dielectric response above 1 MHz. In addition, all SBN compositions show central peaks well documented by different techniques (Brillouin, Raman, neutron scattering) [18–20] and very rich diffuse scattering patterns [21]—related also to disorder at mesoscopic scales—caused mainly by the switching of polar nanodomains (PNDs), by polar fluctuations with correlation lengths of several unit cells, and by anharmonic motion of cations. The half-widths of these central peaks span from 20 to 30 GHz (0.1 meV) [22,23] to 0.7 THz (3 meV) [19], which correspond well to excitations below phonon frequencies found by THz and high-frequency dielectric spectroscopies in several SBN compositions [12,16,17]

All these previous investigations indicate that slower and faster polarization mechanisms are responsible for the phase transition in TTBs and that the coexistence of ferroelectric and relaxor behavior is intimately related to the meso- and microscopic structure of the crystals. In this paper, the high-frequency dynamics of the polarization in the SBN family is reported for a wide concentration range to study the influence of the Sr/Ba substitution on the dielectric response and to elucidate the link between the main excitations and the relaxor/ferroelectric behavior.

II. EXPERIMENTAL

The SBN single crystals of five different compositions ($x = 0.35, 0.51, 0.61, 0.70,$ and 0.81) were grown by the Czochralski method. Details about the growth can be found elsewhere [9]. Samples with assorted geometries were cut from big bulk crystals to fit the experimental requirements of each technique: time-domain THz transmission spectroscopy (TDTTS) from 0.1 to 2.5 THz, waveguide technique from 25 to 50 GHz, high-frequency coaxial line technique (1 MHz–1.8 GHz), and low-frequency dielectric measurements (1 kHz–1 MHz). The real stoichiometry of the crystals and the temperatures of the dielectric permittivity maxima are shown in Table I.

All TDTTS measurements were carried out on $\langle 100 \rangle$ -oriented thin polished plane-parallel plates ($4.5 \times 5 \times 0.05$ mm³) in the temperature range 10–800 K, using a polarized electromagnetic field to measure the response along the c axis, using a custom-made time-domain THz transmission spectrometer [12,17].

Low-frequency dielectric measurements (1 kHz–1 MHz) were performed with a Hewlett-Packard 4192A impedance analyzer. Gold electrodes were sputtered onto the faces of $\langle 001 \rangle$ -oriented plates ($4.5 \times 5 \times 0.8$ mm³), that were heated and then cooled from 600 to 80 K, at a temperature rate of 2 K/min under a probing field of 5 V/cm.

Most dielectric measurements in the high-frequency range (1 MHz–1.8 GHz) were carried out with an Agilent 4291B

TABLE I. Stoichiometry of the SBN crystals and temperatures (T_m in K) of the dielectric permittivity maxima at different frequencies.

Sample name	Stoichiometry	% Sr	T_m ε'_{\max} [1 kHz]	T_m ε'_{\max} [1 MHz]	T_m ε'_{\max} [100 MHz]
SBN-35	$\text{Sr}_{0.35}\text{Ba}_{0.69}\text{Nb}_2\text{O}_{6.04}$	35	462	462	462
SBN-51	$\text{Sr}_{0.51}\text{Ba}_{0.48}\text{Nb}_2\text{O}_{5.98}$	51	380	385	404
SBN-61	$\text{Sr}_{0.61}\text{Ba}_{0.39}\text{Nb}_2\text{O}_6$	61	354	357	392
SBN-70	$\text{Sr}_{0.70}\text{Ba}_{0.26}\text{Nb}_2\text{O}_{5.96}$	70	325	340	380
SBN-81	$\text{Sr}_{0.81}\text{Ba}_{0.17}\text{Nb}_2\text{O}_{5.98}$	81	318	337	370

impedance analyzer, a Novocontrol BDS 2100 coaxial sample cell, and a Sigma System M18 chamber (temperature range 100–570 K) on cooling with a temperature rate of 1 K/min. The majority of the samples were cylinders (of heights $h = 4\text{--}7$ mm, and diameters $d = 0.8\text{--}0.95$ mm) with the polar axis along the main axis, and gold electrodes were sputtered on the bases. Exceptions were SBN-70, measured in the form of a disk ($h = 2$ mm, $d = 3$ mm) and SBN-51 measured as prisms (of thickness ~ 1.84 mm and surface areas ~ 1.9 mm² and ~ 0.55 mm²).

The 25–50-GHz frequency range was covered by two separate waveguided systems on needle-shaped samples. Since the dielectric data vary with temperature significantly, several samples with different cross-section geometry were necessary to maximize the accuracy in different temperature intervals. The samples were hand polished to the particular dimensions by the sand paper. The cross section of the samples varied from 0.07×0.01 to 0.12×0.12 mm² and they were placed in the middle of the wider wall of the waveguide with the c axis perpendicular to it. The frequency band in which the waveguide operates is chosen so that only the fundamental mode H_{10} (also denoted as TE_{10}) can propagate along it. In the region where the sample is placed the H_{10} mode shows a maximum of the electric field, parallel to the c axis of the sample, and a minimum of the magnetic field. A scalar network analyzer Elmika R2400 was used to measure the scalar transmission and reflection coefficients from the sample. The waveguide is equipped with a directional coupler so the incident, transmitted, and reflected waves can be separated. Three diodes were used to measure the electric-field power. One of them is to determine the power provided by the generator, another two are for detecting the transmitted and reflected waves. The complete electro-dynamical model can be found elsewhere [24] and its application to the investigation of ferroelectric systems was already demonstrated [25].

III. RESULTS

The permittivity and losses for different SBN compositions at selected frequencies are presented in Fig. 2. Values for SBN-35 and SBN-81 are the same as in our papers [12,17] and are shown for their proper comparison. The lowest Sr composition (SBN-35, left panels) displays a sharp ferroelectric phase transition, and panels to the right exhibit the enhancing relaxor behavior, manifesting itself mainly in the broadening of the dielectric maxima and in the change of the permittivity maxima position with frequency. Permittivity values above 1 MHz are maximal for SBN-51 and SBN-61,

but on further increase of Sr content the permittivity values decrease, although the relaxor features are still enhanced. The dielectric response $\hat{\varepsilon}_c(\nu, T) = \varepsilon' - i\varepsilon''$ was analyzed on cooling, and the spectra below phonon frequencies were fitted at several temperatures with a model consisting of (i) a sum of Cole-Cole type terms for the excitations below the GHz range, (ii) another Cole-Cole term for the excitation at several GHz, (iii) a damped harmonic oscillator (DHO) for the mode in the THz range, and (iv) the phonon contribution, which was fitted with an overall sum of DHOs:

$$\hat{\varepsilon}(\nu) = \varepsilon'(\nu) - i\varepsilon''(\nu) = \sum_j \frac{\Delta\varepsilon_{0j}}{1 + (i\nu/\nu_{0j})^{1-\alpha_j}} + \frac{\Delta\varepsilon_{\text{GHz}}}{1 + (i\nu/\nu_{\text{GHz}})^{1-\alpha_{\text{GHz}}}} + \frac{\Delta\varepsilon_{\text{THz}}\nu_{\text{THz}}^2}{\nu_{\text{THz}}^2 - \nu^2 + i\gamma_{\text{THz}}\nu} + \sum_{ph,k} \frac{\Delta\varepsilon_k \nu_k^2}{\nu_k^2 - \nu^2 + i\gamma_k \nu}. \quad (1)$$

Here, $\Delta\varepsilon_{0j}$ denotes the dielectric strength of the j th relaxation, ν_{0j} its frequency, and α_j is a real exponent between 0 and 1, which determines the deviation from the pure Debye model for the relaxations and describes the increase of width of the loss peak in the frequency dependences. The same applies to the second term in the GHz range ($\Delta\varepsilon_{\text{GHz}}$, ν_{GHz} , α_{GHz}). In the oscillator term, ν_{THz} and γ_{THz} refer to its frequency and damping constant, and the last term stands for the overall contribution of harmonic phonons at higher frequencies, which is rather low ($\Delta\varepsilon_{ph} \sim 30\text{--}50$), as in other TTBs [26]. In our previous papers, we established that the best way to fit the phonon contribution is to use the generalized four-parameters model [12,17]. However, the phonon contribution to the dielectric response of SBN is not the main subject of the present paper. We took the three-parameters DHO model in order to simplify the treatment and to incorporate a proper approximation of this quantity when fitting the permittivity data measured at lower frequencies. Relevant values of the phonon parameters were taken from our previous papers and then the fits were cut at 10^{13} Hz. The phonons detected by IR and Raman spectroscopy in some SBN crystals can be found here [12,16,17,27], and more details on this important issue will be published elsewhere [28].

In Fig. 3, the frequency dependences of the complex dielectric permittivity are displayed for selected temperatures. For all the compositions, on cooling from ~ 500 K, the low-frequency permittivity rises towards T_m and then decreases monotonically. The maxima of the dielectric loss spectra in the lower panels correspond to the characteristic frequencies of the main excitations found in the crystals. The two main

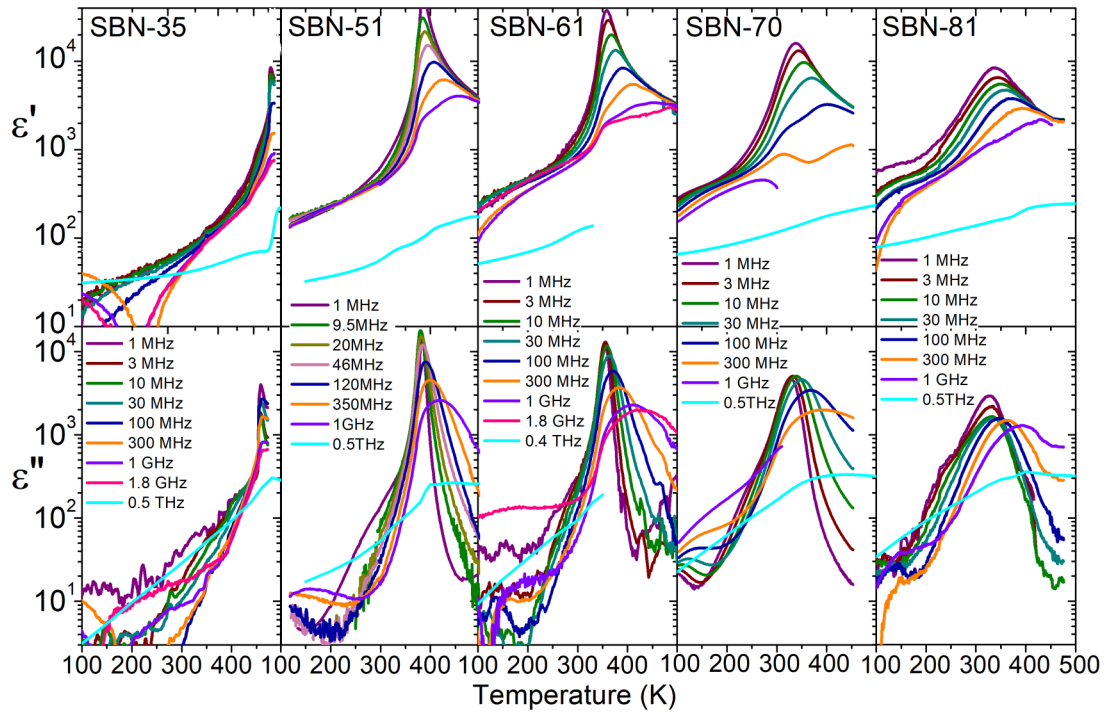


FIG. 2. Temperature dependences of permittivity and dielectric loss of different SBN compositions at high frequencies. Note the logarithmic scales.

maxima, labeled as ν_{01} and ν_{THz} , shift with temperature. On cooling, a third excitation appears in the GHz range, seen mainly at low temperatures. These excitations are present in all the compositions. The most relevant relaxation is present in the MHz–GHz range—labeled as ν_{01} . It relates to the

strongest contribution to the permittivity for all the studied crystals and it shifts towards lower frequencies on cooling. Below 1 MHz there is also another relaxation (ν_{02} in Fig. 3 for SBN-81) but on cooling it goes out from our frequency window, slowing down further into the kHz range and beyond.

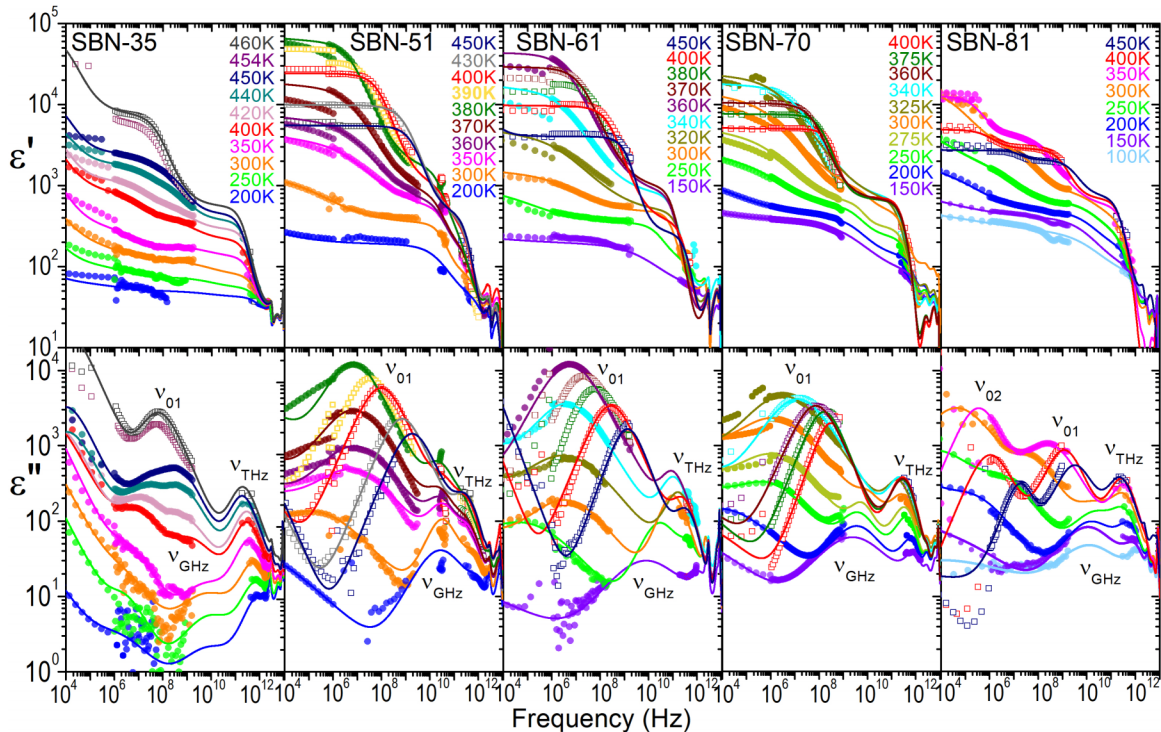


FIG. 3. Frequency dependences of the dielectric permittivity and losses of SBN crystals at selected temperatures from the low-frequency, coaxial line, and TDTTS experiments, together with the fits of the data using Eq. (1). Note the logarithmic scales.

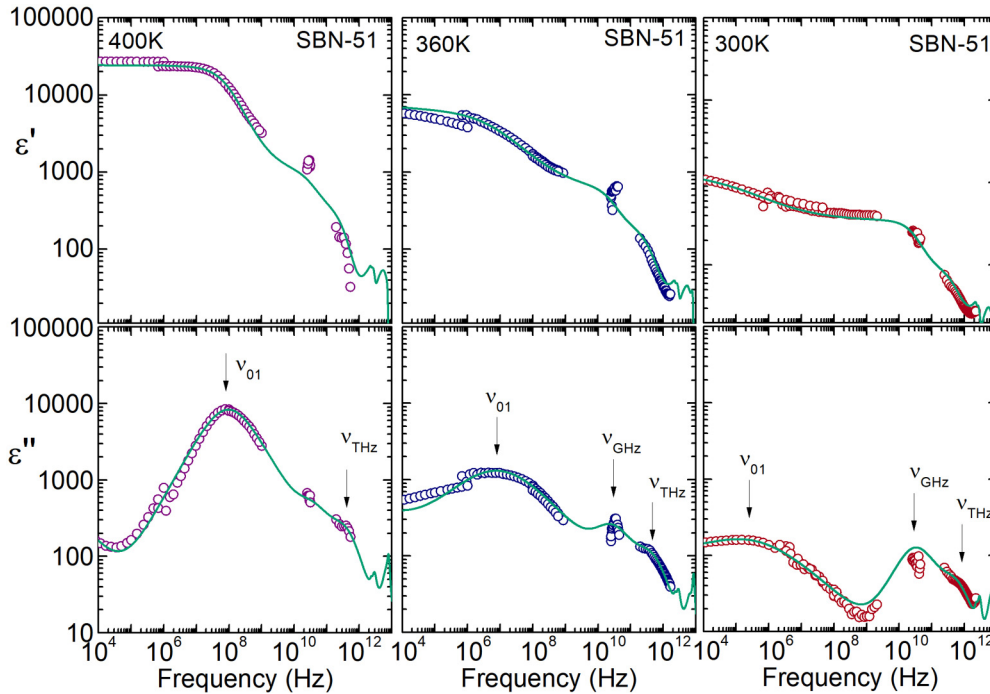


FIG. 4. Frequency dependences of the dielectric permittivity and losses of SBN-51 at selected temperatures from the low-frequency, coaxial line, waveguide, and TDTTS experiments, together with the fits using Eq. (1).

This relaxation was assigned to breathing of polar nanoregions above T_C , [29]. We expect it to be present also in other compositions, but at lower frequencies it is often effectively masked by the electric conductivity. Another excitation (ν_{GHz}) appears above 10 GHz. This excitation accounts for the permittivity values in the GHz range and fits the increase of the dielectric loss data indicated by the slope towards the GHz range in the lower panels of Fig. 3. Finally, the peak located at the THz range—labeled as ν_{THz} —corresponds to the central mode (CM) measured in the THz far-infrared spectra. At higher frequencies, the dielectric response due to phonons becomes detectable.

The SBN-51 crystal was measured also at 30–50 GHz to prove the presence of the extra relaxation between GHz and THz ranges, implied from the experimental data obtained at lower and higher frequency ranges in other compositions. The determination of the complex dielectric permittivity at these frequencies is not trivial, as the complex dielectric permittivity is a nonlinear function of both reflection and transmission modulus, generally written as $\hat{\epsilon}(\nu, T) = \mathcal{F}(|\mathcal{R}|, |\mathcal{T}|)$. This equation is solved by a custom-made program working based on a modified-Newton method. Since the neighboring data obtained by coaxial measurements and TDTTS are unambiguous, the initial parameters for the solver are set according to these data. When multiple roots are available, the correct one can be also chosen according to them.

In Fig. 4, the experimental points and the respective fits with Eq. (1) at selected temperatures are shown in more detail. The measurements at 30–50 GHz indicate that another GHz excitation is actually present at those frequencies; however, it is not straightforward how to fit these data. Several fits were performed to have an estimation about the error bars of the parameters, and delimit the relaxation frequency ν_{GHz} to

10–60 GHz. The experimental data have also larger uncertainties at high temperatures; therefore, it is difficult to know the set on temperature of ν_{GHz} . The waveguide measurements indicate that it might appear already at about 410 K, although it is hard to set a more precise temperature. However, these data definitely showed its presence below 400 K down to low temperatures (Fig. 4), with a nontrivial contribution to the permittivity.

IV. DISCUSSION

A. Excitations below phonon frequencies

1. The central mode

As in SBN the phonon contribution to the permittivity is low (~ 40 – 50), it is necessary to analyze the contribution of excitations below the phonon frequencies to explain the dielectric behavior. This can be done easily from Fig. 3. For all the studied SBN compositions, a CM was found just below the phonon limit, in the THz range, within a frequency range about 0.5–1.5 THz. The temperature dependence of the renormalized CM frequency— $\nu_{r\text{THz}} = \nu_{\text{THz}}^2 / \gamma_{\text{THz}}$, associated with a maximum in the dielectric loss spectrum—displays a minimum [Fig. 5(a)]. Below this minimum, $\nu_{r\text{THz}}$ can be fitted well to the critical law

$$\nu_{r\text{THz}} = a(T_1 - T), \quad (2)$$

with the critical temperature T_1 . The temperature dependence of Eq. (2) does not follow the classic soft-mode behavior, given by the Cochran law $\nu = a(T_C - T)^{1/2}$ [30], but it can be seen as a renormalized Cochran law for overdamped excitations. This supports the fact that this excitation is not related to a harmonic vibration of the crystal lattice, but rather to the

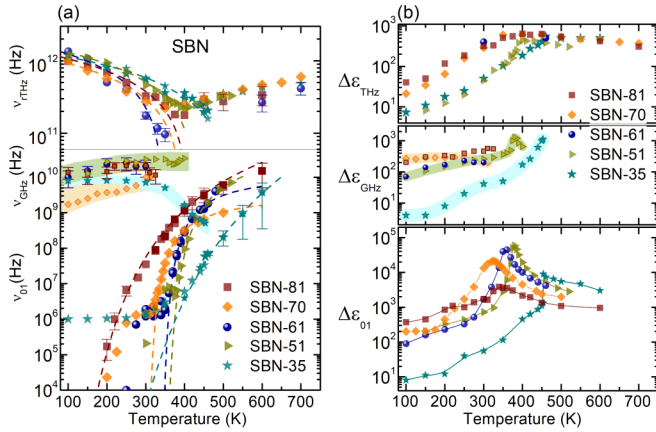


FIG. 5. (a) Temperature dependences of the frequencies of the main excitations found in SBN crystals. Lines correspond to the fits of ν_{THz} and of ν_{01} using Eqs. (2) and (3). (b) Contribution to the permittivity of the main excitations in SBN crystals. The shaded regions refer to the extended error regions for ν_{GHz} and $\Delta\varepsilon_{\text{GHz}}$ found by several fits.

anharmonic rattling or hopping of disordered cations within the channels (Sr, Ba) [19] or inside the oxygen octahedra (Nb).

Values of the fitting parameters of this excitation for the different compositions are set up in Table II, together with the T_C values for the structural phase transition found by measurements of the lattice parameters [31]. It must be noted here that even the relaxor SBN compositions show a structural phase transition into a proper ferroelectric state with macroscopic spontaneous polarization. Therefore, all compositions manifest T_C (the temperature at which the crystal becomes macroscopically ferroelectric) and T_m (maximum of the permittivity). Only for the entirely ferroelectric samples, like SBN-35, $T_C = T_m$. This behavior is in agreement with the idea that each polarization process in SBN has its own characteristic temperature, being more evident for higher Sr content crystals with stronger relaxor behavior.

In our crystals, the temperature T_1 , determined by the softening of ν_{THz} on heating, is higher than T_m for all mixed relaxor compositions, except for SBN-61. This crystal also has the highest a constant, revealing the steepest softening. In general, for the whole SBN series, the temperature behavior of ν_{THz} is somewhat unusual, because the phase transition in SBN has been categorized as of order-disorder type, not showing a soft phonon [12,16,32]. Nevertheless, ν_{THz} displays softening, although towards a critical temperature higher than the actual T_C , even for the ferroelectric crystal SBN-35. Other disordered ferroelectric and relaxors, such as $\text{Pb}(\text{Zr,Ti})\text{O}_3$ or $\text{PbMn}_{1/3}\text{Nb}_{2/3}\text{O}_3$, show this type of temperature-dependent CM as well [33,34], and it was interpreted as the overdamped

or the low-frequency E component of the soft mode, respectively. In SBN, there is no proper soft-phonon mode, as the transition is not of pure displacive type, and the CM is not of phononic origin. On the other hand, it cannot have the same origin as other polar mechanisms at lower frequencies which show different temperature behavior. At very high temperatures, the THz mode ν_{THz} displays a typical CM character but its frequency in the transmission experiment is difficult to assess, due to the high damping; consequently, the fitting is mainly qualitative. However, on cooling it becomes less damped and gets stronger. Then, below the phase transition, it loses its dielectric strength and hardens up to almost the phonon frequencies. All the studied compositions exhibit CMs with very similar frequencies [see Fig. 5(a)], which is in agreement with their assignment to the anharmonic dynamics of Sr or Nb.

2. Sub-THz excitations

Apart from the CM, there are other excitations with lower frequencies which display anomalies on cooling. However, the temperature dependences of each excitation are unlike, as seen in Fig. 5(a), which gives some hints about the different microscopic nature and the length scale of the polarization processes involved. Also, the temperature dependences of the dielectric strength of each excitation are dissimilar, although $\Delta\varepsilon_{\text{THz}}$ and $\Delta\varepsilon_{01}$ display a maximum at $T \sim T_m$ for all the studied compositions [Fig. 5(b)].

In general, the temperature behavior of ν_{01} for the SBN family can be summarized in the following way: at high temperatures in the paraelectric phase, ν_{01} should be present below the CM ν_{THz} . The experiments show that at $T \sim 500$ K its frequency lies already in the GHz range. Then, on cooling, it slows down and broadens over frequency. This relaxation is mainly responsible for the permittivity values measured in the dielectric experiments down to 1 MHz and it has been assigned to polar fluctuations with a correlation length of about 10 nm in the case of SBN-61 [20]. Assuming that their nature is the same in the whole range of SBN compositions, the change of its frequency can suggest that the spatial extent of the polar fluctuations in high Sr content compositions is smaller and progressively becomes larger when lowering the Sr content, as already established by piezoforce microscopy (PFM) experiments [35].

On further cooling, below about 400 K, a third excitation (ν_{GHz}) appears in the frequency range 10–30 GHz. The onset of this relaxation cannot be assessed precisely but it becomes more discernible in the behavior of the right and left wings of the coaxial data and THz data, respectively, especially at lower temperatures. The measurements performed at 30–50 GHz in SBN-51 considerably helped to confirm its presence (see Fig. 4). ν_{GHz} exhibits weaker temperature dependence than

TABLE II. Parameters of Eq. (2) together with the T_C values for several SBN compositions.

	SBN-35	SBN-51	SBN-61	SBN-70	SBN-81
a ($\text{s}^{-1}\text{K}^{-1}$)	$(2.6 \pm 0.1) \times 10^9$	$(3.7 \pm 0.2) \times 10^9$	$(5.0 \pm 0.6) \times 10^9$	$(3.1 \pm 0.4) \times 10^9$	$(3.4 \pm 0.2) \times 10^9$
T_1 (K)	532 ± 12	443 ± 7	344 ± 16	394 ± 22	409 ± 11
T_C (K)	463 ± 1	381 ± 1	346 ± 1	310 ± 1 [SBN – 75]	

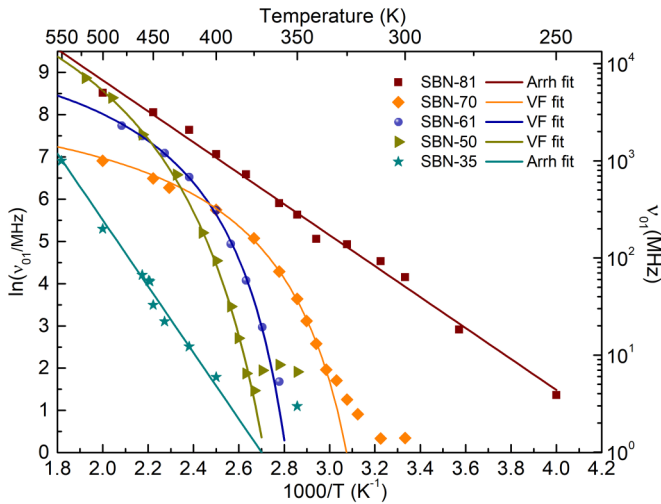


FIG. 6. Vogel-Fulcher fits of the relaxation frequencies ν_{01} for the different SBN compositions, obtained from the maxima of the dielectric loss in Fig. 3.

ν_{01} and correlates well with the presence of diffuse scattering found in SBN-70 [19] and in SBN-61 [36], as well as with a central peak [22] and a relaxation at frequency 5.6×10^{10} Hz [37] found in SBN-75. It also became wider over the frequency spectra at low temperatures, almost merging with the CM. In our previous papers it was labeled as ν_{DW} because it was assigned to oscillations of the small ferroelectric domain walls that appear in SBN crystals [12,17] when the macroscopic polarization develops on cooling. The domain walls should be nanosized, as they are not visible in the PFM experiments [35], and their oscillations fall in the GHz range [38,39]. However, one cannot exclude other mechanisms responsible for ν_{GHz} ; hence, we decided to rename it more generally.

3. The relaxor ferroelectric behavior

The relaxor behavior of a material is often validated by the temperature dependence of the mean relaxation frequency. This dependence can be profitably parametrized by the empiric divergent Vogel-Fulcher law (VF) [40], also known as Vogel-Fulcher-Tammann law [41–43]:

$$\nu = \nu_{\infty} \exp[-E_a/k(T - T_{VF})], \quad (3)$$

where ν_{∞} is the attempt frequency, E_a the activation energy of the relaxation, T_{VF} the characteristic temperature of the relaxing dipoles, and κ the Boltzmann constant. When $T_{VF} = 0$, this equation converts into the classic Arrhenius law $\nu = \nu_{\infty} \exp(-E_a/kT)$. The parametrization of the relaxation ν_{01} at frequencies lower than 1 GHz carried out using Eq. (3)

is shown in Fig. 6 for all compositions, and the parameters obtained from the respective fits are presented in Table III. The mean relaxation frequencies were determined from the positions of the dielectric loss maxima in $\varepsilon''(\nu)$ (Fig. 3), for each composition and temperature.

Figure 6 shows the temperature dependence of the frequency main relaxation, $\nu_{01}(T)$. The fits obtained using Eq. (3) and the parameters shown in Table III are also plotted. Closer inspection reveals a fundamental qualitative difference between the two extreme compositions SBN-35 and SBN-81, which show a clear Arrhenius behavior with $T_{VF} = 0$, and the intermediate compositions presenting a characteristic temperature $T_{VF} > 0$. In SBN-35, the Arrhenius behavior is expected, as it is a “conventional” ferroelectric crystal with ferroelectric domains of ~ 500 nm in size, but SBN-81 is relaxor with PND of less than 100 nm in size [35]. The reason for the absence of finite T_{VF} could be that the PNDs associated with ν_{01} are so small that they cannot actually freeze. A similar behavior was reported for $\text{Ba}(\text{Zr,Ti})\text{O}_3$ relaxor compositions [44]. In SBN T_{VF} lies below the actual phase transition temperature for all compositions and the concept of freezing is not attainable because of the presence of real ferroelectric domains below T_C .

The analysis based on Eq. (3) is not always unambiguous in order to get reliable parameters, especially in case of ceramics [45]. However, in our case, crystals of all investigated compositions were grown under the same conditions and, in addition, our frequency span is broad enough. Therefore, some meaningful information can be obtained from the experimental data. The three samples with intermediate compositions reveal finite T_{VF} temperatures, but this is not the case for the two ending members (SBN-35 and SBN-81). The attempt frequencies ν_{∞} are much higher for these samples: they reach the phonon range for SBN-35, and the GHz limit for 51 to 70% of Sr, respectively. Moreover, the activation energy E_a has the lowest values (about 0.023 eV) for SBN-61 and SBN-70. It is worth mentioning here that the respective parameters reported on SBN-75 in the literature are not completely unanimous. For instance, some dielectric experiments manifest the Arrhenius behavior of a relaxation with $\nu_{\infty} = 1850 \times 10^{12}$ Hz and $E_a = 0.45$ eV [37], although another study found at high temperatures $\nu_{\infty} = 800 \times 10^{12}$ Hz, $E_a = 0.4$ eV [46]. These values are similar to the ones we found in SBN-81 [$\nu_{\infty} = (10.2 \pm 3.0) \times 10^{12}$ Hz and $E_a = 0.319 \pm 0.009$ eV]. On the other hand, the VF behavior of a relaxation with $\nu_{\infty} = 36 \times 10^9$ Hz, $E_a = 0.013$ eV, and $T_{VF} = 311$ K was reported [47], which is more in agreement with our values for SBN-70 [$\nu_{\infty} = (3.8 \pm 0.8) \times 10^9$ Hz, $E_a = 0.0226 \pm 0.002$ eV, and $T_{VF} = 293 \pm 3$ K]. These discrepancies could be due to the different frequency ranges explored in the given experiments. The values of T_m

TABLE III. Vogel-Fulcher parameters obtained from the fits in Fig. 6 with Eq. (3).

	SBN-35	SBN-51	SBN-61	SBN-70	SBN-81
E_a/k (K)	7850 ± 300	646 ± 76	270 ± 4	263 ± 24	3700 ± 100
E_a (eV)	0.68 ± 0.03	0.056 ± 0.007	0.0232 ± 0.0003	0.0226 ± 0.002	0.319 ± 0.009
T_{VF} (K)	0	315 ± 5	330 ± 0 fixed	293 ± 3	0
ν_{∞} (Hz)	$1642 \pm 900 \times 10^{12}$	$(173 \pm 65) \times 10^9$	$(14.0 \pm 0.5) \times 10^9$	$(3.8 \pm 0.8) \times 10^9$	$(10.2 \pm 3.0) \times 10^{12}$

obtained from the real part of the susceptibility follows the activated dynamic scaling law predicted for the random-field Ising model [48], with $T_a[E_a/k] = 320$ K ($E_a = 0.03$ eV), $T_c[T_{VF}] = 299$ K, and $f_0[\nu_\infty] = 5.8 \times 10^9$ Hz. These values are in agreement with the ones in Table III.

Our permittivity data up to the THz limit indicate the presence of several polarization mechanisms contributing to the dielectric response of SBN at high frequencies. Their dynamics, as observed at high frequencies (above 1 MHz), is related to the mesoscopic structure emerging in the SBN crystals, and their temperature evolution in the subphonon frequency range has to be intimately linked to the evolution of these formations, like polar fluctuations, PNDs, oxygen octahedral tilts, and cationic disorder [7,19–21]. They contribute to the permittivity in different length scales and, consequently, in different frequency and temperature ranges. Their interplay is responsible for the intricate and thus unique relaxor-ferroelectric behavior of SBN. Our findings seem to prove that the mechanism of the ferroelectric phase transition in the SBN solid solution is complex and cannot be simply classified into the displacive type or order-disorder type, as there is no proper soft-phonon mode driving the transition or a single slowing-down mechanism. All these high-frequency polarization mechanisms were not earlier discerned in SBN-61 [16] because of the huge dielectric contribution of the ν_{01} relaxation, which effectively masked other relaxations, and due to the absence of reliable enough data collected in the GHz and THz ranges. We refitted the data on SBN-61 crystal with Eq. (3) and obtained the same parameters for ν_{01} ; however, the fit of the THz data was significantly improved because the multiple-excitations model appears to be more suitable here. In this way we could also resolve ν_{GHz} and ν_{THz} at low temperatures, and the resulting fitting parameters become more consistent than the previous ones [16].

B. The two polarization subsystems

The multiple polarization mechanisms behavior of SBN is partially due to the presence of two polarization subsystems related to the two types of NbO_6 octahedra. Recent *ab initio* molecular-dynamics calculations at different temperatures [15] showed that Nb(1) atoms inside the linking octahedra (Fig. 1) are substantially off-centered along the polar axis at temperatures well above T_c contributing to a robust local polarization which does not depend much on the chemical environment. The other niobium atoms, Nb(2), in the octahedra of the perovskite-unit network (Fig. 1), are more affected by the Sr substitution within the pentagonal channels. The simulations revealed that when larger amount of Sr is present in the crystal, tilts of higher magnitude are induced in the structure, because the crystal lattice has to adapt to the smaller size of Sr in comparison to Ba. The larger tilts are those of the Nb(2)O_6 octahedra surrounding a vacancy in the squared channels (possibly coupled to shifts of Sr atoms in the pentagonal channels), and the central Nb(2) atoms move away to compensate the local charges, with a substantial *ab*-plane displacement component.

We calculated the Nb shifts along the *c* axis and their contribution to the spontaneous polarization P_s for both types of octahedra Nb(1)O_6 and Nb(2)O_6 , following structural data

in different compositions [7,8,15]. Their individual atomic contribution to P_s was obtained using the formula [49,50]

$$P_s[\text{Nb}] = \sum_i \frac{m_i \times \Delta z_i \times Q_i e}{V}, \quad (4)$$

where m_i is the multiplicity of Nb sites, Δz_i the relative shift along the *c* axis, Q_i the valence of Nb (+5), e the charge of the electron, and V the unit-cell volume.

The shifts of the Nb(1) and Nb(2) atoms and their two different contributions to P_s are depicted in Fig. 7. Figure 7(a) illustrates the displacements of the two different Nb atoms, along the *c* axis from the centers of their respective octahedra in various compositions available in the literature. There are two clear trends: Nb(1) shifts more than Nb(2), and the shifts decrease with Sr content, especially for Nb(2). This fact affects considerably the development of the polarization. The right panel [Fig. 7(b)] depicts the cumulative contribution of Nb(1) and Nb(2) to P_s , and the total P_s measured experimentally in some crystals [2].

The graph describes well the fact that the overall polarization from Nb decreases when Sr content increases, as found in the total P_s by pyroelectric measurements [2]. Nevertheless, a closer look at the graph reveals that this effect is primarily due to the Nb(2) atoms, because the polarization from Nb(1) is about $3\text{--}5 \mu\text{C}/\text{cm}^2$. On the contrary, polarization arising from Nb(2) diminishes from $\sim 15 \mu\text{C}/\text{cm}^2$ in SBN-33 to $\sim 7\text{--}10 \mu\text{C}/\text{cm}^2$ for Sr contents above 0.65. As the Nb(2) shifts in the perovskite-unit sublattice are related to the fluctuating part of the polarization, this part of the polarization is maximal for SBN-33, and the overall P_s from Nb atoms as well. We have also added in Fig. 7 the results of first-principle structural optimization for SBN-30, SBN-50, and SBN-80.

The calculations were done using the program SIESTA [51] with the same setting as described in our previous work [15]. The SBN-50 $2 \times 2 \times 8$ supercell was altered to satisfy the stoichiometry of the other two compositions. The distribution of atomic species and vacancies was quasirandom with the stoichiometry being roughly preserved also in the smaller subsections of the calculation box. The atomic coordinate optimization was performed with the conjugate gradient method until the forces acting on atoms were smaller than 0.075 eV/Å. In all three cases, the supercells were fully polarized as an initial condition and stayed so in the optimized state. The resulting Nb-O shifts (averaged over pairs created by 320 Nb atoms in the supercell) are larger than those extracted from the published structures, which is presumably due to the fact that distortions could develop freely in a relatively large supercell without any symmetry constraints. Nevertheless, the corresponding polarization values stay within the range observed experimentally [2]. The same trend as in the case of the experimental structures is observed; the Δz shifts of Nb(2) atoms are more suppressed than those of Nb(1) in the case of Sr-rich compositions. In the case of SBN-80 in-plane shifts are ~ 0.15 Å, already bigger than those in the *z* direction.

The uneven shifts of the two Nb atoms create two different polarization regions of dissimilar lengths and volumes which also display different temperature behaviors. Nb(2) shifts along the polar axis are smaller and less correlated, as a result of the Nb(2)O_6 tilts in the perovskite units. On the contrary,

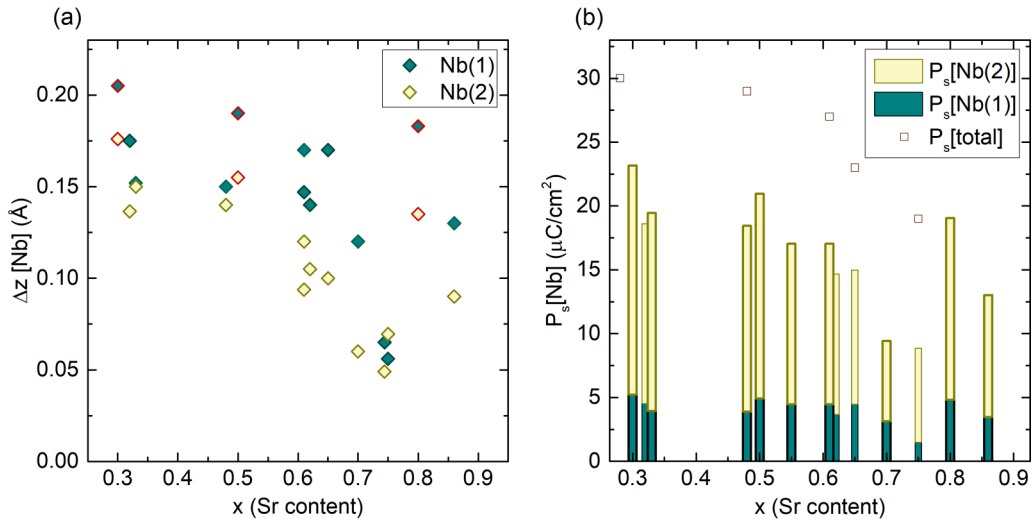


FIG. 7. (a) Shifts of the two Nb atoms at room temperature according to structural data [7,8,15], and (b) their contribution to the spontaneous polarization. Results of the first-principle calculations for $x = 0.3, 0.5$, and 0.8 (shown in red) are added for comparison (see text for details).

the linking octahedra $\text{Nb}(1)\text{O}_6$ are isolated from each other, thus more rigid, and the Nb atom inside is more akin to shift along the c axis contributing more to the polarization. Because of this, there are at least two correlation lengths associated with the polarization mechanisms (related to each type of Nb), and this probably manifests also in the dielectric response, having contributions from both.

Our simulations showed that the effect of a Sr vacancy in the channels is to promote tilts and deformations in the perovskite subunits of the crystal lattice around the vacancy and, consequently, disturb the Nb atoms within the octahedra. However, the built-in disorder in the oxygen octahedra network due to the random cationic occupation is the cause of the shifts of Nb atoms mainly in the ab plane, instead of being shifted along the c axis, enhancing thus the relaxor behavior. The compound $(\text{Ca}, \text{Ba})\text{Nb}_2\text{O}_6$, with the smaller atom Ca instead of Sr, shows no relaxor properties, which is presumably due to the absence of random cationic occupation in the channels [52].

A definitive microscopic assignment of the relaxations found in SBN would be somehow speculative, and probably ν_{01} and ν_{GHz} have contribution of the two types of sublattices. However, ν_{01} , the main relaxation found, is responsible for the dielectric anomaly at T_m in the GHz–MHz range, as clearly demonstrated by its dielectric strength $\Delta\epsilon_{01}$ [Fig. 5(b)]. Its frequency slows down in all compositions on cooling and its underlying microscopic/mesoscopic mechanism corresponds to the polar fluctuations found in neutron transverse diffuse scattering [20]. Sole Nb(1)-O chains are probably not strong enough to produce the predominant permittivity contribution, as they are isolated. On the other hand, the large Nb(1) shifts indicate that these chains will have a substantial correlation length and their dynamics should have an important impact on the lowest-frequency relaxation ν_{01} .

The ν_{GHz} excitation, then, should be assigned to a mechanism with shorter correlation length, because of its higher frequency. It could be also related to the oscillations of small domain walls that appear eventually in all the compo-

sitions when lowering the temperature. However, its dielectric strength is larger in the relaxor samples, $\Delta\epsilon_{\text{GHz}} \sim 400$ in SBN-81 and only 50 in SBN-35 at 300 K [see Fig. 5(b)]. This might suggest that ν_{GHz} is related to the fluctuating part of the polarization due to Nb(2) shifts, more affected by occupational disorder.

Indications of the presence of two different correlations lengths were found already in SBN-61 by PFM [35], where mesoscopic regions of quasistatic correlated polarization coexists with dynamic ones of smaller scale. Also very recently, diffuse scattering in SBN-60 [53] revealed the coexistence of two different kinds of local ordering with different correlation lengths and shapes of the correlation functions.

Finally, the CM ν_{THz} is caused by the anharmonic rambling or hopping of cations, Sr and probably also Nb, which is quite displaced in the ab plane in the relaxor samples, as found in our first-principles calculations [15]. Above T_C its dielectric strength is similar for all the compositions $\Delta\epsilon_{\text{THz}} \sim 500$ –600, but below T_C it is about one order of magnitude stronger in the relaxor samples [$\Delta\epsilon_{\text{THz}} \sim 50$ for SBN-35 and SBN-51, and $\Delta\epsilon_{\text{THz}} \sim 300$ –400 for SBN-61, 70, and 81, as seen in Fig. 5(b)]. The absence of a classic soft-phonon mode in this system [12,16,17,27] is probably due to the inhomogeneous arrangement of the oxygen octahedra in the unit cell, where perovskite subunits containing Nb(2) atoms are bonded with linking octahedra containing Nb(1) atoms. This kind of perturbation in the arrangement of the octahedra network most likely prevents the global evolution of the soft mode like in typical perovskite systems.

V. CONCLUSIONS

The SBN family exhibits an intrinsic ferroelectric nature that gets mixed with an enhancing relaxor behavior when Sr content increases. The ferroelectric phase transition shows a complex behavior in which several excitations play their roles. The discovered excitations correspond to different polarization mechanisms, with various correlation lengths

of mesoscopic order and characteristic frequencies between MHz and THz, contribute to the overall dielectric response. This supports the coexistence of displacive and order-disorder scenarios.

The temperature evolution of the dielectric behavior of SBN could be described as follows: A strong excitation, present in the THz range at very high temperatures, splits on cooling into several components: a soft CM in the THz range (related to anharmonic motion of cations) [19], an intermediate excitation (labeled ν_{GHz}) of mixed character, and a relaxation (labeled ν_{01}) associated with polar fluctuations of the forming PNDs. The relaxation ν_{01} is the strongest and it is associated with polar fluctuations of nanometric size that grows into PND on cooling. Its dielectric contribution is maximal for Sr contents about 0.5–0.61. The ν_{GHz} excitation could be due to polar fluctuations of shorter correlation lengths, but also due to oscillations of tiny domain walls that appear even in the relaxor samples. It is stronger in relaxor crystals, which show higher degree of disorder and thus more intense diffuse scattering.

The effect of the Sr increase on the relaxor behavior is indirect and mediated via disorder in the oxygen octahedra network which causes disorganized shifts of Nb atoms inside the octahedra. As the Nb(2) displacements along the *c* axis are smaller in the relaxor samples, they contribute less to the macroscopic polarization in these crystals.

ACKNOWLEDGMENTS

This work was supported by the Czech Science Foundation (Project No. 16–09142S) and by Operational Programme Research, Development and Education financed by European Structural and Investment Funds and the Czech Ministry of Education, Youth and Sports (Project No. SOLID21 - CZ.02.1.01/0.0/0.0/16_019/0000760). Access to computing facilities owned by parties and projects contributing to the NationalGrid Infrastructure MetaCentrum, provided under the Program No. Cesnet LM2015042, is appreciated.

-
- [1] M. H. Francombe, The relation between structure and ferroelectricity in lead barium and barium strontium niobates, *Acta Crystallogr.* **13**, 131 (1960).
- [2] A. M. Glass, Investigation of the electrical properties of $\text{Sr}_{1-x}\text{Ba}_x\text{Nb}_2\text{O}_6$ with special reference to pyroelectric detection, *J. Appl. Phys.* **40**, 4699 (1969).
- [3] M. D. Ewbanks, R. R. Neurgaonkar, and W. K. Cory, Photorefractive properties of strontium-barium niobate, *J. Appl. Phys.* **62**, 374 (1987).
- [4] J. Dec, W. Kleemann, T. Woike, and R. Pankrath, Phase transitions in $\text{Sr}_{0.61}\text{Ba}_{0.39}\text{Nb}_2\text{O}_6$: Ce^{3+} : I. Susceptibility of clusters and domains, *Eur. Phys. B* **14**, 627 (2000).
- [5] R. A. Cowley, S. N. Gvasaliya, S. G. Lushnikov, B. Ressler, and G. M. Rotaru, Relaxing with relaxors: A review of relaxor ferroelectrics, *Adv. Phys.* **60**, 229 (2011).
- [6] P. B. Jamieson, S. C. Abrahams, and J. L. Bernstein, Ferroelectric tungsten bronze-type crystal structures. I. Barium strontium niobate $\text{Ba}_{0.27}\text{Sr}_{0.73}\text{Nb}_2\text{O}_6$, *J. Chem. Phys.* **48**, 5048 (1968).
- [7] T. S. Chernaya, B. A. Maksimov, T. R. Volk, L. I. Ivleva, and V. I. Simonov, Atomic structure of $\text{Sr}_{0.75}\text{Sr}_{0.25}\text{Nb}_2\text{O}_6$ single crystal, *Phys. Solid State* **42**, 1716 (2000).
- [8] S. Podlozhenov, H. A. Graetsch, J. Sneider, M. Ulex, M. Wolecke, and K. Betzler, Structure of strontium barium niobate $\text{Sr}_x\text{Ba}_{1-x}\text{Nb}_2\text{O}_6$ (SBN) in the composition range $0.32 < x < 0.82$, *Acta Crystallogr. B* **62**, 960 (2006).
- [9] T. Lukasiewicz, M. A. Swirkowicz, J. Dec, W. Hofman, and W. Szyrski, Strontium–barium niobate single crystals, growth and ferroelectric properties, *J. Cryst. Growth* **310**, 1464 (2008).
- [10] G. Burns, J. D. Axe, and D. F. O’Kane, Raman measurements of $\text{NaBa}_2\text{NbO}_5$ and related ferroelectrics, *Solid State Commun.* **7**, 933 (1969).
- [11] J. R. Oliver, R. R. Neurgaonkar, and L. E. Cross, A thermodynamic phenomenology for ferroelectric tungsten bronze $\text{Sr}_{0.6}\text{Ba}_{0.4}\text{Nb}_2\text{O}_6$ (SBN:60), *J. Appl. Phys.* **64**, 37 (1988).
- [12] E. Buixaderas, M. Kempa, V. Bovtun, C. Kadlec *et al.*, Multiple polarization mechanism across the ferroelectric phase transition of the tetragonal tungsten bronze SBN-35, *Phys. Rev. Mater.* **2**, 124402 (2018).
- [13] H. A. Graetsch, Large structural modulations in the relaxor ferroelectric and intermediate state of strontium rich members ($x > 0.6$) of the $\text{Sr}_x\text{Ba}_{1-x}\text{Nb}_2\text{O}_6$ (sbn) solid solution series, *J. Solid State Chem.* **246**, 167 (2017).
- [14] G. H. Olsen, U. Aschauer, N. A. Spaldin, S. M. Selbach, and T. Grande, Origin of ferroelectric polarization in tetragonal tungsten-bronze-type oxides, *Phys. Rev. B* **93**, 180101(R) (2016).
- [15] M. Pasciak, P. Ondrejko, J. Kulda P. Vanek, J. Drahokoupil, G. Steciuk, L. Palatinus, T. R. Welberry, H. E. Fischer, J. Hlinka, and E. Buixaderas, Local structure of relaxor ferroelectric $\text{Sr}_x\text{Ba}_{1-x}\text{Nb}_2\text{O}_6$ from a pair distribution function analysis, *Phys. Rev. B* **99**, 104102 (2019).
- [16] E. Buixaderas, M. Savinov, M. Kempa, S. Veljko *et al.*, Infrared and dielectric spectroscopy of the relaxor ferroelectric $\text{Sr}_{0.61}\text{Ba}_{0.39}\text{Nb}_2\text{O}_6$, *J. Phys.: Condens. Matter* **17**, 653 (2005).
- [17] E. Buixaderas, C. Kadlec, M. Kempa, V. Bovtun, M. Savinov, P. Bednyakov, J. Hlinka, and J. Dec, Fast polarization mechanism in the uniaxial tungsten-bronze relaxor SBN-81, *Sci. Rep.* **7**, 18034 (2017).
- [18] F. M. Jiang, J. H. Ko, and S. Kojima, Central peaks and Brillouin scattering in uniaxial relaxor single crystals of $\text{Sr}_{0.61}\text{Ba}_{0.39}\text{Nb}_2\text{O}_6$, *Phys. Rev. B* **66**, 184301 (2002).
- [19] F. Prokert, Neutron scattering studies on strontium barium niobate, *Phys. Status Solidi B* **113**, 239 (1982).
- [20] P. Ondrejko, M. Kempa, J. Kulda, B. Frick, M. Appel, J. Combet, J. Dec, T. Lukasiewicz, and J. Hlinka, Dynamics of Nanoscale Polarization Fluctuations in a Uniaxial Relaxor, *Nanoscale* **13**, 167601 (2014).
- [21] M. Pasciak, M. Kopecky, J. Kub, J. Fabry, J. Dec, P. Ondrejko, J. Hlinka, and E. Buixaderas, X-ray diffuse scattering observations for $\text{Sr}_x\text{Ba}_{1-x}\text{Nb}_2\text{O}_6$ single crystals with $x = 0.35$ and 0.81 , *Phase Transitions* **91**, 969 (2018).

- [22] S. Tsukada and S. Kojima, Gigahertz range relaxation in relaxor ferroelectric $\text{Sr}_{0.75}\text{Ba}_{0.25}\text{Nb}_2\text{O}_6$, *Jpn. J. Appl. Phys.* **49**, 09ME03 (2010).
- [23] J. H. Ko, Intrinsic and extrinsic central peaks in the Brillouin light scattering spectrum of the uniaxial ferroelectric relaxor $\text{Sr}_{0.61}\text{Ba}_{0.39}\text{Nb}_2\text{O}_6$ *Appl. Phys. Lett.* **91**, 082903 (2007).
- [24] J. Grigas, *Microwave Dielectric Spectroscopy of Ferroelectrics and Related Materials* (Gordon and Breach, New York, 1996).
- [25] J. Grigas, A. Brilingas, and V. Kalesinkas, Microwave and millimetre wave dielectric spectroscopy of ferroelectrics, *Ferroelectrics* **107**, 61 (1990).
- [26] E. Buixaderas, V. Porokhonskiy, A. Pashkin, M. Savinov, and J. Petzelt, Broad-band dielectric spectroscopy of $\text{Ba}_2\text{NaNb}_5\text{O}_{15}$ single crystal, *Eur. Phys. B* **30**, 319 (2002).
- [27] E. Buixaderas, I. Gregora, J. Hlinka, J. Dec, and T. Lukasiewicz, Raman and IR phonons in ferroelectric $\text{Sr}_{0.35}\text{Ba}_{0.69}\text{Nb}_2\text{O}_{6.04}$ single crystals, *Phase Transitions* **86**, 217 (2013).
- [28] E. Buixaderas and J. Dec, Phonons and relaxations in unfilled tetragonal tungsten-bronzes, in *Perovskites and Other Framework Structure Materials: New Trends and Perspectives*, edited by M. B. Smirnov and P. Saint-Grégoire, OAJ Materials and devices Vol. 4(2) (Collaborating Academics IP, France, in press).
- [29] J. Dec, W. Kleemann, V. V. Shvartsman, D. C. Lupascu, and T. Lukasiewicz, From mesoscopic to global polar order in the uniaxial relaxor ferroelectric $\text{Sr}_{0.8}\text{Ba}_{0.2}\text{Nb}_2\text{O}_6$, *Appl. Phys. Lett.* **100**, 052903 (2012).
- [30] W. Cochran, Dynamical, scattering and dielectric properties of ferroelectric crystals, *Adv. Phys.* **18**, 157 (1969).
- [31] R. Paszkowski, K. Wokulska, T. Łukasiewicz, and J. Dec, Temperature dependence of lattice parameters of SBN single crystals in the vicinity of their structural phase transitions, *Cryst. Res. Technol.* **48**, 413 (2013).
- [32] S. N. Gvasaliya, R. A. Cowley, L. I. Ivleva, S. G. Lushnikov, B. Roessli, and A. Zheludev, Phase transition of the uniaxial disordered ferroelectric $\text{Sr}_{0.61}\text{Ba}_{0.39}\text{Nb}_2\text{O}_6$, *J. Phys.: Condens. Matter* **26**, 185901 (2014).
- [33] E. Buixaderas, I. Gregora, M. Savinov, J. Hlinka, L. Jin, D. Damjanovic, and B. Malic, Compositional behavior of Raman active phonons in $\text{Pb}(\text{Zr}_{1-x}\text{Ti}_x)\text{O}_3$ ceramics, *Phys. Rev. B* **91**, 014104 (2015).
- [34] D. Nuzhnyy, J. Petzelt, V. Bovtun, M. Kempa, S. Kamba, J. Hlinka, and B. Hehlen, Infrared, terahertz, and microwave spectroscopy of the soft and central modes in $\text{Pb}(\text{Mg}_{1/3}\text{Nb}_{2/3})\text{O}_3$, *Phys. Rev. B* **96**, 174113 (2017).
- [35] V. V. Shvartsman, W. Kleemann, T. Łukasiewicz, and J. Dec, Nanopolar structure in $\text{Sr}_x\text{Ba}_{1-x}\text{Nb}_2\text{O}_6$ single crystals tuned by Sr/Ba ratio and investigated by piezoelectric force microscopy, *Phys. Rev. B* **77**, 054105 (2008).
- [36] P. Ondrejko, M. Kempa, M. Savinov, P. Bednyakov *et al.*, Electric-field influence on the neutron diffuse scattering near the ferroelectric transition of $\text{Sr}_{0.61}\text{Ba}_{0.39}\text{Nb}_2\text{O}_6$, *Phase Transitions* **89**, 808 (2016).
- [37] O. Kersten, A. Rost, and G. Schmidt, Dielectric dispersion of relaxor ferroelectrics SBN 75 and PLZT 8/65/35, *Phys. Status Solidi A* **76**, 495 (1983).
- [38] E. Buixaderas, V. Bovtun, M. Kempa, D. Nuzhnyy, M. Savinov, P. Vanek, I. Gregora, and B. Malic, Lattice dynamics and domain wall oscillations of morphotropic $\text{Pb}(\text{Zr}, \text{Ti})\text{O}_3$ ceramics, *Phys. Rev. B* **94**, 054315 (2016).
- [39] G. Arlt, Ferroelastic domain walls as powerful shear wave emitters at microwaves, *Ferroelectrics* **172**, 95 (1995).
- [40] R. Pirc and R. Blinc, Vogel-Fulcher freezing in relaxor ferroelectrics, *Phys. Rev. B* **76**, 020101(R) (2007).
- [41] H. Vogel, Das Temperaturabhängigkeitsgesetz der Viskosität von Flüssigkeiten, *Phys. Z.* **22**, 645 (1921).
- [42] G. S. Fulcher, Analysis of Recent Measurements of The Viscosity of Glasses, *J. Am. Ceram. Soc.* **8**, 339 (1925).
- [43] G. Tammann and G. Hesse, Die Abhängigkeit der Viskosität von der Temperatur bei unterkühlten Flüssigkeiten, *Z. Anorg. Allg. Chemie* **156**, 245 (1926).
- [44] J. Petzelt, D. Nuzhnyy, M. Savinov, V. Bovtun *et al.*, Broadband dielectric spectroscopy of $\text{Ba}(\text{Zr}, \text{Ti})\text{O}_3$: Dynamics of relaxors and diffuse ferroelectrics, *Ferroelectrics* **469**, 14 (2014).
- [45] A. Rotaru and F. D. Morrison, Vogel-Fulcher analysis of relaxor dielectrics with the tetragonal tungsten bronze structure: $\text{Ba}_6\text{MnNb}_9\text{O}_{30}$, *J. Therm Anal. Calorim.* **120**, 1249 (2015).
- [46] A. V. Baldenkov, I. M. Buzin, N. A. Morozov, and A. I. Rukabishnikov, Dielectric spectra of sodium barium niobate single crystals, *Fiz. Tverd. Tela* **23**, 2376 (1981).
- [47] S. Ganesamoorthy, I. Bhaumik, R. Bhatt, A. K. Karnal *et al.*, A Comparative Study of Dielectric Relaxation in $\text{Sr}_{0.61}\text{Ba}_{0.39}\text{Nb}_2\text{O}_6$ and $\text{Sr}_{0.75}\text{Ba}_{0.25}\text{Nb}_2\text{O}_6$ Single Crystals, *Jpn. J. Appl. Phys.* **47**, 1012 (2008).
- [48] J. Dec, W. Kleemann, and T. Lukasiewicz, Critical slowing down in the single crystalline relaxor SBN75, *Phase Transitions* **79**, 505 (2006).
- [49] J. D. Axe, Ionic displacements and spontaneous polarization in displacive ferroelectrics, *Solid State Commun.* **5**, 413 (1967).
- [50] Y. Shimakawa, Y. Kubo, Y. Nakagawa, S. Goto, T. Kamiyama, H. Asano, and F. Izumi, Crystal structure and ferroelectric properties of $\text{ABi}_2\text{Ta}_2\text{O}_9$ ($A = \text{Ca}, \text{Sr}, \text{and Ba}$), *Phys. Rev. B* **61**, 6559 (2000).
- [51] J. M. Soler, E. Artacho, J. D. Gale, A. García, J. Junquera, P. Ordejón, and D. Sánchez-Portal, The SIESTA method for ab initio order- N materials simulation, *J. Phys.: Condens. Matter* **14**, 2745 (2002).
- [52] M. Eßer, M. Burianek, P. Held, J. Stade *et al.*, Optical characterization and crystal structure of the novel bronze type $\text{Ca}_x\text{Ba}_{1-x}\text{Nb}_2\text{O}_6$, *Cryst. Res. Technol.* **38**, 457 (2003).
- [53] P. Yu. Vanina, S. B. Vakhrushev, A. A. Naberezhnov, and A. A. Bosak, Multiscale local ordering in the prototypical uniaxial relaxor $\text{Sr}_{0.6}\text{Ba}_{0.4}\text{Nb}_2\text{O}_6$ single crystal at room temperature, *J. Phys.: Condens. Matter* **31**, 175401 (2019).